

# Polymeric microneedle-based platform enables simultaneous delivery of cancer immunomodulatory drugs and detection of biomarkers in the skin

**Pere Dosta**

Harvard Medical School

**Núria Puigmal**

Harvard Medical School

**Alexander M. Cryer**

Harvard Medical School

**Alma Lorena Rodríguez**

Harvard Medical School

**Ella Scott**

Harvard Medical School

**Ralph Weissleder**

Harvard Medical School

**Miles A. Miller** (✉ [miles.miller@mgh.harvard.edu](mailto:miles.miller@mgh.harvard.edu))

Harvard Medical School

**Natalie Artzi** (✉ [nartzi@mit.edu](mailto:nartzi@mit.edu))

Harvard Medical School

---

## Research Article

**Keywords:** microneedles, immunotherapy, cancer, poly(beta-amino ester)s, theranostics

**Posted Date:** May 18th, 2022

**DOI:** <https://doi.org/10.21203/rs.3.rs-1643439/v1>

**License:** © ⓘ This work is licensed under a Creative Commons Attribution 4.0 International License.

[Read Full License](#)

---

**Version of Record:** A version of this preprint was published at Theranostics on January 1st, 2023. See the published version at <https://doi.org/10.7150/thno.73966>.

# Abstract

## Background

Intratumorally injected immune-modulating therapies have advanced to clinical trials over the last few years. Despite some reports on efficacy of different approaches, there remains a need for improved delivery strategies and non-invasive monitoring of anti-tumor effects.

## Methods

This work reports a microneedle (MN) platform capable of simultaneous delivery of immune activators and collection of sample fluids to monitor therapeutic responses. While either approach has shown promise, the combination of the two into one theranostic platform has been previously untested. MNs were synthesized out of hyaluronic acid (HA) and loaded with a model immunomodulatory drug, CpG nanoparticles (TLR9 agonist), for cancer therapy. The therapeutic response was monitored by temporal analysis of entrapped immune cells in the MNs following their retrieval and digestion.

## Results

Transdermal delivery of CpG-NPs induced anti-tumor immune responses in multiple syngeneic mouse cancer models. CpG-loaded MN stimulated innate immune cells and reduced tumor growth. Intravital microscopy showed spatiotemporal co-localization and sustained deposition of CpG-NPs delivered with MN in tumors. Analysis of sampled cells within the MNs revealed similar immune signature to that seen in the bulk tumor homogenate. In addition, immune surveillance using MNs showed an increase in the infiltrates of effector T cells after treatment.

## Conclusions

We validated the theranostic potential of our hydrogel-based MNs in dually supporting transdermal drug delivery and temporal monitoring of tumor immune composition in a minimally invasive manner. This platform has the potential to deliver a range of combination therapies while detecting biomarkers.

## Introduction

Microneedles (MN) have emerged as promising platforms in the drug delivery field thanks to advantageous features including self-administration, needle-free penetration, and minimally-invasive access to a complex immune reservoir unique to the skin [1,2]. For cancer, MNs have been proposed to deliver anti-tumoral molecules (such as chemotherapeutics, cytokines, and nucleic acids) either in the form of free drugs or as nanoformulations [3,4]. Applying these paradigms for immunotherapies is particularly interesting [5,6] as it can potentially avoid detrimental systemic toxicities [6–8]. MNs have

also been recently investigated for minimally-invasive extraction of interstitial skin fluid (ISF) to allow early diagnosis and clinical monitoring of a wide range of pathologies, including cancer [9–11]. ISF comprises 75% of all extracellular fluid and contains biomarkers that can reflect physiological function and correlate with disease state [12–15]. For cancer, surveillance of immune infiltrates and soluble biomarkers of the tumor microenvironment (TME) have been proposed to assess responsiveness to immunotherapy [11,16]. Yet there is little data on whether this is indeed of clinical value. Previous reports establishing correlations between ISF and patient prognosis had done so using models such as breast cancer [17–19], yet we envision that the use of ISF for diagnostic purposes could possess a higher translational potential when targeting superficial tumors such as melanoma, which may offer easy access with minimally-invasive platforms such as MNs.

Despite their promise for therapeutic and diagnostic purposes, MNs encompassing both abilities within the same platform –as a theranostic tool– have rarely been explored. Combining both compartments requires designs that allow for high drug loading efficiency and maximal sampling volume of biomarkers such as nucleic acids, proteins, metabolites, or cells [11,20–23]. To efficiently and gently isolate ISF biomarkers that have accumulated in MNs – especially cells –dissolving MNs is needed to release their contents for further analysis [22,23]. Here, we present the design and application of an adjuvant-loaded hydrogel-based MN platform for cancer theranostics. This device delivers an immunomodulator to augment innate anticancer immunity while subsequently sampling ISF for surveillance of the TME in response to the therapy.

Unmethylated cytosine-phosphate-guanine (CpG) oligonucleotides (ODNs) are well-described innate immune effectors capable of instigating potent anti-tumor responses by selectively engaging with toll-like receptors (TLRs) expressed by innate immune cells [24,25]. However, *in vivo* delivery of CpG continues to be challenging due to high hydrophilicity and rapid degradation [26]. To overcome these limitations, our theranostic MNs were loaded with nanoparticles (NPs) derived from poly ( $\beta$ -amino ester)s (PBAEs) [27–31] that encapsulate the CpG-ODNs (herein referred to as CpG-NPs) to protect them from degradation and enhance cellular internalization [26,32]. Here, we demonstrate that transdermal delivery of CpG-NPs via MNs alters the functional state of the tumor immune infiltrate, reduces tumor growth, and increases overall survival in syngeneic melanoma and colorectal murine cancer mouse models. Intravital microscopy (IVM) confirmed the ability of the MNs to localize the CpG-NPs inside the tumor. In addition, these MNs permitted subsequent temporal ISF sampling from tumor-adjacent skin. Analysis of the ISF cellular fraction confirmed a correlation with the immune changes observed in the TME in response to the immunotherapy, therefore establishing a basis for using MNs as a theranostic platform for simultaneously perturbing the TME and monitoring such disturbances in response to the therapy.

## Results And Discussion

# Engineered Hydrogel-based MNs for cancer treatment

A dual-function MN patch platform for delivery of drug molecules and subsequent ISF sampling was designed based on a hyaluronic acid (HA) MN platform [23], engineered here to incorporate CpG-ODNs as a model immune stimulant. In this study, we aimed to leverage the theranostic potential of our MN platform for anti-cancer purposes by (1) delivering nano-encapsulated drugs in the vicinity of tumors to suppress tumor growth while simultaneously (2) sampling ISF from the TME to monitor the response to the therapy (Fig. 1a). TLR9 agonists, including CpG ODN 1826 used here and related compounds, have been tested as intralesional therapies with well-described mechanisms of action [33,34]. Therefore CpG-NPs were used as a model agent to prove TME responsiveness to TLR9 agonist treatment.

To construct the MNs, the HA polymeric backbone was modified with cysteamine dihydrochloride to include primary amine groups (for hydrogel formation) and disulfide bonds (for hydrogel digestion when incubated with a reducing agent (tris (2-carboxyethyl) phosphine (TCEP))) (**Figure S1**). To form the MNs, the modified HA polymer containing primary amines was crosslinked with 8-Arm-NHS-PEG containing a succinimidyl functional group, allowing for spontaneous hydrogel formation (**Figure S2**). Once the MN hydrogel backbone was formed, CpG-NPs were incorporated by centrifugation, and the MN patch was finalized by the addition of a Poly Lactic-co-Glycolic Acid (PLGA) back layer. Following patch retrieval, the MNs can be digested on-demand in less than 5 minutes to recover the biomarkers present in ISF (both cells and soluble molecules) for subsequent analysis, integrating an *ex vivo* diagnostic compartment to the MN patch.

Formulations of TLR agonists such as CpG-ODNs have been long shown to inhibit tumor growth in pre-clinical studies [33,34]. Yet, their nature –being single-stranded, short synthetic DNA molecules– makes them particularly prone to premature clearance by endonucleases if delivered in free form. Given the ability of PBAE polymers to encapsulate and deliver nucleic acids such as plasmid DNA[28,29] microRNA[30], and siRNA[31], we selected the tri-arginine-modified PBAE polymer (C6-CR3)[27] (**Figure S3 and S4**) as a model delivery vehicle to protect the ODNs and enhance their cellular internalization. To establish the C6-CR3-to-CpG ratio required for complete complexation of the nucleic acids, we used a gel retardation assay (**Figure S5a**). Here, the presence of cationic groups in the CR3-C6 polymer allowed electrostatic binding to the negatively charged phosphate groups of the CpG-ODNs. The gel retardation assay revealed that CpG-ODNs migration was impeded at weight ratios of 50:1 C6-CR3:CpG. Therefore, we used this formulation throughout the rest of the study. Analysis by dynamic light scattering (DLS) confirmed the encapsulation of the CpG into monodisperse particles ( $PDI = 0.12 \pm 0.02$ ) with a hydrodynamic diameter of  $63 \pm 9$  nm. CpG-NPs displayed a positive surface charge (zeta potential =  $23 \pm 2$  mV) attributed to the high density of protonated groups in the polypeptides (Fig. 1b). Storage stability of the CpG-NPs was also monitored by DLS, confirming that their diameter remained relatively unchanged for more than a week at room temperature (**Figure S5b**).

We next investigated the ability of CpG-NPs to be internalized by the murine TLR9-expressing HEK 293 cells (Fig. 1c). Cells were incubated with varying concentrations of fluorescent CpG-NPs (from 0.001 nM to 1000 nM) for 24h in complete growth medium, confirming over 90% of NP internalization at 10 nM and half-maximal effective concentration (EC<sub>50</sub>) of 0.78 nM. CpG-NP cytotoxicity was only observed at ~ 20-

fold higher concentrations than those required to stimulate TLR9 activity, as observed by an MTS cell proliferation assay when incubating the CpG-NPs with the HEK293 TLR9 reporter cells (**Figure S6**). We also studied the ability of CpG-NPs to stimulate the NF- $\kappa$ B response, being the central signaling pathway for the induction of pro-inflammatory responses [35]. Following 24-hour incubation with HEK293 cells expressing murine TLR9, we observed that the CpG-NPs prompted the highest activation, with up to a 4-fold increase compared to free CpG (Fig. 1d). We confirmed that the NF- $\kappa$ B response was explicitly triggered by the CpG motifs in the ODN 1826 TLR9 agonist since its control counterpart (CpG-Crt-NP) containing CpC dinucleotides yielded low levels of activation. We also confirmed that CpG-NPs were active once released from the MNs (**Figure S7**).

We next examined the properties of the theranostic MN platform and its behavior when integrating the NPs in the hydrogel matrix for delivery into the dermal milieu surrounding the tumors. We confirmed that MNs could efficiently disrupt the stratum corneum in the tumor area in mice (as evidenced by the presence of micro-conduits lengthening about 600  $\mu$ m deep) (Fig. 1e). To confirm the successful release of CpG-NPs from the MNs, we next assessed the release kinetics of fluorescently labeled CpG-NPs (Fig. 1f) when incubated under physiologically relevant conditions (pH = 7.4, 37°C) *in vitro*. We confirmed that 70% of the CpG-NPs were released within the first 24 h of incubation and that a plateau was achieved by 72 h. Release studies *in vivo* showed that half of the NP cargo was delivered from the MNs after 24 h (46%  $\pm$ 12%, n = 10 mice). Briefly, MNs retrieved from mice were digested, and the fluorescence associated with the remaining CpG-NPs was compared to the baseline levels recorded from MNs that had not been implanted. In light of these findings, a total of 2  $\mu$ g CpG/MN patch was loaded in subsequent *in vivo* studies to reach a therapeutic target of 1  $\mu$ g CpG per mouse following 24 h of MN administration. Finally, quantification of the mechanical strength of the MNs by compression testing did not reveal significant differences between empty MN patches and those loaded with the CpG-NPs (Fig. 1g), supporting our previous findings where the inclusion of other therapeutics such as chemokines or cytokines in the MN matrix did not have an impact on its physical properties [23].

### **CpG-NPs enhance activation in innate immune cells.**

We next studied the capability of CpG-NPs to activate murine bone marrow-derived dendritic cells (BMDCs) and bone marrow-derived macrophages (BMDMs). BMDCs and BMDMs were generated following published guidelines[36] that involved culturing isolated murine bone marrow cells in GM-CSF or M-CSF, respectively (see Methods). BMDCs phenotype was confirmed as CD11c<sup>+</sup> MHCII<sup>+</sup> and BMDMs phenotype was confirmed as CD11b<sup>+</sup> F4/80<sup>+</sup> by flow cytometry. We first studied the ability of BMDMs and BMDCs to efficiently internalize CpG-NPs, and observed EC50s of 2.6 nM and 22.5 nM, respectively (Fig. 1c). To test the downstream cellular response to CpG-NPs, BMDCs were treated for 24h with CpG-NPs or CpG-Crt-NP, and the expression of cell activation markers was determined by flow cytometry. A 10% increase of CD86<sup>+</sup>MHCII<sup>hi</sup> (major histocompatibility complex class II, high expression) population was observed in BMDCs treated with CpG-NPs compared to CpG-Crt-NPs. In addition, no significant CD86<sup>+</sup>MHCII<sup>hi</sup> population increase was observed when comparing the levels of activation in CpG-Crt-NPs-treated BMDCs and the untreated ones, corroborating that TLR9-specific activation only occurred in the

presence of CpG (Fig. 2a, 2b). Similar results were observed in BMDMs since an increase in the ratio of pro-inflammatory to anti-inflammatory macrophages was observed when BMDMs were treated with 10nM of CpG-NP compared to untreated or CpG-Crt-NP controls (Fig. 2c) (pro-inflammatory M1-like BMDMs were defined as CD86<sup>+</sup> cells and anti-inflammatory M2-like as CD206<sup>+</sup> cells). These results confirmed that CpG-NPs stimulate maturation and activation of BMDCs and BMDMs. Following TLR engagement, activated BMDMs are known to produce a wide range of cytokines and chemokines to promote anti-tumor immunity [37]. To test that, we used an antibody multi-analyte flow assay kit to analyze the supernatant of CpG-NP-treated macrophages. An increase in leukocyte chemoattractant (MCP-1, CXCL1, and CXCL10), as well as pro-inflammatory cytokine (TNF- $\alpha$ ), was observed (Fig. 2d). Immunosuppressive IL-10 cytokine was also upregulated, like as has been reported following TLR stimulation in DCs [38].

### **CpG-NPs suppress tumor growth when delivered via the dual-function MN platform.**

Following the characterization of the MN platform, we pursued *in vivo* studies in mice to validate the theranostic ability of the MN platform. We first used an orthotopic murine model of melanoma (B16-F10) as a clinically relevant, superficial tumor offering easy access *via* the transdermal route. First, we focused on the therapeutic effects of the MN platform by examining the ability of the CpG-NPs to instigate antitumor immunity when delivered with the MNs. Five days-post tumor inoculation, B16-tumor bearing mice were administered MNs loaded with CpG-NPs (CpG-NP MNs) or empty MNs for the control group, where the therapeutic regimen consisted of treatment every three days for five cycles (q3dx5). Treatment with CpG-NP MNs resulted in a significant delay in tumor growth (Fig. 3b) and a corresponding increase in the survival time compared to the control group (Fig. 3c). The therapeutic benefit of CpG-NP MNs when delivered transdermally was evidenced by the 3-fold lower tumor volume at the end of the study ( $\approx 800$  mm<sup>3</sup> in the control group (Fig. 3d) versus  $\approx 200$  mm<sup>3</sup> in the treatment group (Fig. 3e)). In addition, we observed that 1  $\mu$ g of CpG-NPs per mouse was well tolerated as no apparent body weight loss was observed during the treatment period (**Figure S8**). In agreement with previous reports [33], the nanoencapsulation of the CpG induces therapeutic effects at a much lower dose than when delivered as free drugs intratumorally [39], validating the benefit of using NPs for nucleotide delivery.

### **MNs release CpG-NPs in the TME for tumor suppression, as confirmed by IVM.**

After confirming the potential of the MNs in a clinically relevant melanoma model, we then studied the spatiotemporal distribution of CpG-NP in the TME when delivered using the MNs by confocal *in vivo* (intravital) microscopy (IVM). We used the syngeneic MC38 cancer model with growth characteristics and fluorescent protein expression ideal for intravital microscopy. MC38 tumor cells expressed H2B-mApple nuclear-localized fluorescent protein and were implanted into dorsal skinfold window chambers (DSWC) on C57BL/6J mice [40]. MNs containing fluorescent AF647-labeled CpG-NPs were applied to tumor-bearing mice roughly 7 days after tumor induction. After 24h, the MN patch was removed for imaging (Fig. 4a), which revealed a relatively homogeneous distribution of CpG-NPs from the patch into the neighboring tumor tissue and around the MN puncture sites (Fig. 4b). Single-cell analysis of CpG-NP

uptake indicated accumulation in H2B-mApple<sup>+</sup> tumor cells and non-malignant phagocytic host cells consistent with known morphology and localization of tumor-associated macrophages in this model[40] (Fig. 4c).

We next studied the therapeutic efficacy of transdermal delivery of CpG NPs using the subcutaneous MC38 colon cancer model. Tumors responded similarly to orthotopic B16-F10 tumors: treatment with CpG-NP MNs inhibited tumor growth (Fig. 4d,e) and extended overall humane survival (Fig. 4f). IVM also revealed a robust tumor response using the DSWC, where the loss of fluorescent signal reflected a loss of viable mApple<sup>+</sup> tumor cells over time after a single CpG-NP MNs application (Fig. 4g,h). IVM also showed sustained CpG-NP deposition after MN patch removal that lasted for more than 24 hours after removal but mainly was gone by nine days post-treatment (Fig. 4g). The DSWC used for IVM allows more efficient access to tumor tissue since the top layer of skin is removed for imaging; nonetheless, these data collectively show that local and transdermal delivery of CpG-NP by MN patches is effective in slowing tumor growth in multiple superficial tumor models.

### **Analysis of the therapeutic potential of MNs for modulating the tumor microenvironment**

To understand the mechanisms by which the transdermal delivery of CpG-NPs resulted in enhanced antitumor activity, we performed an immunohistochemical analysis of the TME once the treatment in the MC38 model was completed (CpG-NP MNs, q3dx5). In agreement with the macroscopic findings, immunohistochemical staining for H&E and Ki-67 showed less actively proliferating cells in tumors treated with CpG-NP MNs than the control group administered empty MNs (Fig. 5a). In addition, we characterized the composition and the phenotype of the immune cell populations in the TME and tumor-draining lymph nodes (tdLNs) in MC38 tumor-bearing mice two days after a single administration of CpG-NP MNs, with a particular focus on early immune responders. Expression of CD80 by DCs (CD11c<sup>+</sup> MHCII<sup>+</sup>) in the TME and tdLNs was significantly increased in the animals treated with CpG-NP loaded MNs (Fig. 5b). A similar trend was observed for the macrophages (CD11b<sup>+</sup> F4/80<sup>+</sup>), where an increase in CD86 expression in treated mice compared to the control group receiving empty MNs was observed (Fig. 5c). These results support that CpG TLR-agonists are potent stimulators of DC and macrophages maturation and drive the expression of co-stimulatory receptors, including CD80 or CD86 [41]. Increased frequencies of natural killer (CD45<sup>+</sup>NK<sup>+</sup>) cells were measured in tumors administered with CpG-NP MNs, in agreement with prior literature showing TLR-agonists such as CpG motifs can induce NK cell lytic activity to support anti-tumor immunity [41,42] (Fig. 5d). We also observed by flow cytometry that T cell infiltrates in the tumors were low at baseline (accounting for less than 1% of all CD45<sup>+</sup> cells), which is consistent with prior reports [43,44] (Fig. 5e). Nonetheless, we registered higher frequencies of CD4<sup>+</sup> T cell infiltrates in the treated group compared to the control group. Lastly, we examined how transdermal delivery of CpG-NPs affected proinflammatory cytokines and chemokines that are known to mediate innate and adaptive immune cell activation. Analysis of the tumor lysates confirmed that CpG-NP MNs increased the expression of IFN- $\gamma$  in the TME compared to control mice receiving empty MNs. In addition, tumors treated with CpG-NP MNs showed increased expression of leukocyte chemokines, such as MCP-1

and CXCL1, and pro-inflammatory cytokines (IL-1 $\beta$ ) responsible for immune cell recruitment [45] (Fig. 5f). Overall, these results demonstrate the immunomodulatory potential of the MN platform, leading to a pro-inflammatory TME phenotype.

### **Non-invasive cell sampling using HA-based MNs allows continuous monitoring of immunotherapy response.**

We next investigated the diagnostic capacity of the MN platform and its ability to extract ISF for minimally-invasive monitoring of the TME. We aimed to utilize the MN platform to serially monitor the changes in the TME profile in ISF, which we hypothesized would shift from immunosuppressive to pro-inflammatory following TLR engagement, while also understanding the correlations with the TME from tumors. Following CpG-NPs therapy administration, empty MNs were applied for 24 hours and digested to analyze proximal responders of TLR stimulation, such as phagocytic macrophages known to accumulate CpG-NP and express TLR9 (Fig. 6a, left). The whole MN matrix was composed of highly swellable and digestible HA hydrogel that allowed us to capture and analyze roughly 1000 CD45<sup>+</sup> cells per patch in a theoretical volume of 3 mm<sup>3</sup>. Next, we were able to further gate this cellular subset by flow cytometry to examine the cellular frequencies of the main contributors to anti-tumor immunity, such as macrophages, and compare them with those found after tumor biopsy (Fig. 6a, right). Flow cytometric quantification of the cellular suspensions recovered from MNs on day two post-treatment confirmed an increase in the percentage of macrophages (CD11b<sup>+</sup> F4/80<sup>+</sup> CD45<sup>+</sup>) in MNs recovered from treated mice than in those sampling the control group (Fig. 6b, 6c). This same trend was observed in the corresponding tumors, which registered increased frequencies of macrophages in mice administered with CpG-NPs (Fig. 6b, 6c), supporting a correlation between cells extracted from MN patches and the bulk TME in response to the immunotherapy.

In a second study, we focused on monitoring the adaptive immune responses that may evolve more gradually, particularly examining effector and helper T cells. Here, CpG-NP MNs were serially administered following the same therapeutic regimen as for the efficacy studies (q3dx5). Cellular changes in the MN-sampled ISF were analyzed as before by flow cytometry (Fig. 6d). Mainly, we focused on the population of infiltrating tumor-infiltrating lymphocytes, using the CD8<sup>+</sup>/CD4<sup>+</sup> T cell ratio as a prognostic biomarker of responsiveness to immunotherapy which some claim provides higher accuracy than clinicopathologic characteristics [46–48]. Analysis of the MN-sampled TME infiltrate revealed an increase in the CD8<sup>+</sup> T cell population in treated mice compared to the control group, which was evident in all the samples analyzed over time (Fig. 6e). Also, an increase in the CD8<sup>+</sup>/CD4<sup>+</sup> ratio following immunotherapy was observed, although not statistically significant, compared to untreated mice (pooled frequencies from day 11 and day 14 post-treatment initiation) (Fig. 6f). Here, the correlation between the T cell signature in the TME and the response to therapy could only be established qualitatively due to the low frequencies of effector T cells inherent to the MC38 model [49]. Despite the experimental constraints—which we hypothesize could be avoided if profiling T-cell-inflamed tumors—we confirmed the potential of the diagnostic arm of the MN platform as it allowed identifying cellular subsets such as effector T cells that were scarce in the

TME. To our knowledge, correlating the TME composition by MN analysis with the bulk tissue state of the tumor has only been pursued soluble biomarkers (such as proteins and nucleic acids [17–19]). Instead, we describe the use of cellular biomarkers sampled from ISF to infer the state of the tumor and prognosis following treatment by minimally invasive means. These results support the potential use of our HA-based MNs to sample the immune cell profile in the TME. The correlation between the immune signature of MN-extracted cells and that of the bulk tumors for DC, macrophage, and T cell populations supports the potential of this platform for future theranostic avenues.

## Conclusions

We have leveraged our dual-function MN platform for minimally invasive immunotherapy administration and analytical sampling in the context of cancer management. The hydrogel matrix of the MNs was loaded with NPs encapsulating an immunomodulatory agent (CpG-ODNs), enabling their localization at the tumor site as observed by IVM. Following MN administration, the tumor burden was reduced when treating an orthotopic melanoma cancer model and a subcutaneous colorectal cancer model.

Mechanistic studies confirmed the activation of DCs and macrophages in response to TLR engagement and the remodeling of the TME towards a stimulatory state, which was evidenced by the increased levels of pro-inflammatory cytokines and chemokines in tumor lysates. MNs facilitated longitudinal monitoring of the changes in the TME, focusing on the innate arm of the immune system in early time points followed by the adaptive responses. We reported an increase in macrophages in MN-sampled ISF after treatment that correlated with the immune profile in tumors, as well as an average increase in the infiltrates of effector and helper T cells. We foresee that integrating therapeutic and diagnostic functionalities of hydrogel-based MNs in a single, theranostic patch will open up prospective clinical avenues for enhanced patient management, offering minimally invasive intervention and allowing for multiplex analysis of cellular biomarkers involved in anti-tumor immunity.

## Materials And Methods

### Materials

All reagents and solvents were purchased from Sigma Aldrich unless otherwise stated. Sodium hyaluronate (60kDa) was obtained from LifeCore Medical with a purity of at least 95%. NHS-terminated 8-arm PEG was purchased from Creative PEG Works. Microneedle PDMS custom-made molds (11 X 11 needles with a height 600  $\mu\text{m}$ , base width of 300  $\mu\text{m}$ , and tip to tip spacing of 600  $\mu\text{m}$ ) were obtained from Blueacre Technology. Arginine peptide (H-Cys-Arg-Arg-Arg-NH<sub>2</sub>) was obtained from CPC Scientific with a purity of at least 90%. ODN 1826 (CpG) and ODN 2138 (CpG-Crt) were purchased from Invivogen.

*Synthesis of pBAE polymers functionalized with arginine polypeptide:* Polymers were synthesized in accordance with previous work [27]. PBAE polymerization was performed by mixing 5-amino-1-pentanol (0.426 g, 4.1 mmol), hexylamine (0.422 g, 4.1 mmol), and 1,4-butanediol diacrylate (2.0 g, 9.1 mmol) under magnetic stirring at 90°C for 24 h. Next, acrylate moieties were end-capped with thiol-terminated

arginine peptide at 1:2.1 pBAE:peptide molar ratio in dimethyl sulfoxide (DMSO). The mixture was stirred overnight at room temperature, and the resulting polymer was precipitated with a mixture of diethyl ether and acetone (70:30 v/v). Arginine modified pBAE polymer (C6-CR3) structure was confirmed by  $^1\text{H-NMR}$  (400 MHz Varian NMR spectrometer).

*CpG retardation assay.* To assess CpG complexation, different CpG to C6-CR3 ratios (w:w) (between 1:1 and 400:1) were studied. CpG-NP were freshly prepared and loaded in 4% E-Gel Precast Agarose Gels (Thermo Fisher), run following the manufacturer's instructions, and visualized in fluorescence mode.

### **Formation of CpG-NPs**

NPs were generated by mixing equal volumes of CpG at  $0.4 \text{ mg mL}^{-1}$  and C6-CR3 polymer at  $20 \text{ mg mL}^{-1}$  in sodium acetate buffer (AcONa) at 12.5 mM, followed by 5 min incubation at room temperature (RT). Next, this mixture was nano precipitated with 2.5 volumes of PBS and incubated for 20 min at RT to form nanoparticles. The final CpG-NPs were concentrated by centrifugal filtration (10kDa MWCO) and sterilized by filtration at  $0.22 \mu\text{m}$ .

### **Biophysical characterization of CpG-NP**

Dynamic light scattering (DLS) determined the size and surface charge.  $100 \mu\text{L}$  of CpG-NP were diluted with  $900 \mu\text{L}$  of PBS and analyzed using a Zetasizer Nano ZS equipped with a He-Ne laser ( $\lambda = 633 \text{ nm}$ ) at a scattering angle of  $137^\circ$  (Malvern Instruments Ltd, United Kingdom).

*Synthesis of Amino-modified hyaluronic acid (HA-SS-NH<sub>2</sub>) polymer.* The HA-SS-NH<sub>2</sub> polymer was synthesized following a previously described procedure [23]. Briefly, 60 kDa-sodium hyaluronate (1% w/v in MES buffer) was activated with N-(3-(dimethylamino)propyl)carbodiimide (EDC) and N-hydroxysuccinimide (NHS) at a 1:4:2 molar ratio and reacted at room temperature for 30 minutes. The activated hyaluronic acid (HA) was then mixed with Cysteamine Dihydrochloride at a 1:10 molar ratio and reacted at room temperature for 12 h. HA-SS-NH<sub>2</sub> was purified by dialysis, freeze-dried, and stored at  $-20^\circ\text{C}$ . HA-SS-NH<sub>2</sub> molecular structure was characterized by  $^1\text{H-NMR}$  using D<sub>2</sub>O as a solvent (400 MHz Varian NMR spectrometer).

### **HA-based MN fabrication**

MNs were produced in concordance with our previous work [23], using custom-made molds consisting of an 11 x 11 array of negative MNs projections, each with a height of  $600 \mu\text{m}$  and a radius of  $150 \mu\text{m}$ . First, HA-SS-NH<sub>2</sub> polymer (10% w/v in phosphate buffer, pH = 7.4) was cast on top of the molds by centrifugation at 4200 rpm. The excess polymer was carefully removed, and molds were freeze-dried. Then, an 8-arm-PEG-NHS crosslinker (10% w/v in phosphate buffer, pH = 7.4) was added to the HA-SS-NH<sub>2</sub> polymer and cast by centrifugation under the same conditions. Next, a solution containing CpG-NPs and glycine ( $10 \text{ ng mL}^{-1}$ ) was deposited carefully on top of the projections area of the mold, put in a vacuum for 2 minutes, and centrifugated for 1 minute. Immediately after, a polymeric backing layer of

PLGA (Resomer® RG 505, Poly(D,L-lactide-co-glycolide), Sigma-Aldrich, USA) at 15% (w/v) dissolved in acetonitrile was added dropwise until covering the whole area of the mold. Finally, CpG-NP loaded MNs were dried at room temperature for 12 h, peeled off the molds carefully, and stored at room temperature.

## **Cell Lines**

Mus musculus skin melanoma (B16-F10 from ATCC) and Colon carcinoma (H2B-mApple MC38, developed and described previously [40], were maintained in Dulbecco's minimum essential medium (DMEM) supplemented with 10% (v/v) fetal bovine serum (FBS), 100 U/mL penicillin and 100 µg/mL streptomycin, 2 mM L-glutamine. HEK-Blue mTLR9 cells (InvivoGen) were similarly maintained with the addition of 100 µg/ml of Normocin™ and Zeocin™ and 30 µg/ml of blasticidin. B.

## **Bone marrow-derived dendritic cell (BMDC) and Bone marrow-derived macrophage (BMDM) isolation**

The tibias and femurs of female C57BL/6 mice (aged 8–12 weeks) were isolated and flushed to harvest bone marrow and obtain a progenitor cell population. To generate BMDMs, 4-6x10<sup>6</sup> bone marrow cells were cultured in non-tissue culture-treated T175 flasks with DMEM/F12 supplemented with 10% (v/v) FBS, 1% (v/v) P/S, 5% (v/v) GlutaMAX and recombinant murine macrophage-colony-stimulating factor (M-CSF, 20 ng/mL). The flasks were supplemented with the additional medium on day three and day six. BMDMs phenotype was confirmed as CD11b<sup>+</sup> F4/80<sup>+</sup> by flow cytometry. To generate BMDCs, 2x10<sup>6</sup> bone marrow cells were added to non-tissue culture-treated Petri dishes and cultured in 10 mL of RPMI-1640 supplemented with 10% (v/v) FBS, 1% (v/v) and recombinant murine granulocyte-macrophage colony-stimulating factor (GM-CSF, 20 ng/mL) from Biolegend, 10 mL more of which was added on day three. On day six and every other day after that until use, 10 mL of consumed medium was centrifuged and replaced with 10 mL of fresh medium. To collect the cells for use in experiments, BMDMs were detached using Accumax™ (Sigma), and BMDCs were loosely adherent and could be collected by simple washing. BMDCs phenotype was confirmed as CD11c<sup>+</sup> MHCII<sup>+</sup> by flow cytometry.

## **In vitro evaluation of CpG-NP activity**

HEK-Blue mTLR9 cells were seeded in 96-well plates at 2 x 10<sup>5</sup> cells per well and incubated with the CpG-NP, CpG-Crt-NP, free CpG, or free CpG-Crt at concentrations ranging from 0 nM to 6 nM. At 24 h post-treatment, NF-κB activity was determined using the HEK-Blue Detection™ reagent (InvivoGen) according to the manufacturer's instructions.

## **Cell viability**

HEK-Blue mTLR9 cells were seeded in 96-well plates at 2 x 10<sup>5</sup> cells per well. Cells were treated with different concentrations of CpG-NPs and CpG-Crt-NP for 24h, and cell viability was assessed using the MTS assay (Promega) as instructed by the manufacturer. Cells were incubated for up to 2 h, and absorbance was measured at 490 nm using a plate reader.

## Cell internalization studies

HEK-Blue mTLR9 cells, BMDCs, BMDMs were seeded in 24-well plates at  $1 \times 10^5$  cells per well and incubated with fluorescently labeled CpG-NP at CpG concentrations ranging from 0.0001 to 100 nM. After 4 h, excess CpG-NPs were removed, cells were washed, trypsinized, and fixed with 4% (v/v) paraformaldehyde for 10 min. CpG-NPs internalization was determined by flow cytometry.

*Primary immune cell activation using CpG-NPs:* BMDCs or BMDMs were seeded in 24-well plates at  $1 \times 10^5$  cells per well and incubated with CpG-NP or CpG-Ctr-NP at 10nM. After 24 h, the supernatant was removed, and cells were then collected and analyzed by flow cytometry. The following antibodies were used: CD11c BV421 (clone N418), MHCII BV605 (clone M5/114.15.2), CD80 FITC (clone 16-10A1), CD86 PE (clone GL-1), F4/80 BUV395 (clone T45-2342), CD11b BV421 (clone M1/70), CD86 FITC( clone GL-1), CD80 APC (clone 16-10A1), CD206 PE (clone C068C2). Live cells were gated using LIVE/DEAD™ (Thermo Fisher) near-IR (cat. no. L34976). In addition, CCL2 (MCP-1), CXCL1 (KC), CXCL10 (IP-10)), TNF- $\alpha$  and IL10 were analyzed from the BMDM supernatant using a custom Legendplex™ panel (BioLegend) as per the manufacturer's instructions.

## Analysis of the mechanical strength of the HA-derived MNs

Mechanical properties of the MNs when empty or CpG-loaded were measured using a micro-force test station with a mechanical sensor (3400 Series, Instron, USA). MN patches were placed on the surface of the platform with the needle-like projections facing up. The displacement and force applied to the MNs were recorded from the moment the sensors touched the uppermost tip of the MNs until a maximum force of  $\approx 100$  N was reached. Force-travel curves of MNs arrays were obtained by correlating the compressive strain or displacement (%) with the compressive stress (kPa), and Young's modulus was determined from the slope (GPa).

*Study of CpG-NP release kinetics from the MNs:* To assess the release of CpG-NPs from the HA MNs, CpG-NPs were conjugated with Alexa Fluor 647 before the microneedle fabrication. CpG-NP-loaded MNs were placed in Eppendorf tubes, immersed with PBS (1 mL), and incubated under rotation at 37°C. 100  $\mu$ l of releasing media was replaced at a predetermined time point, and fluorescence of the release NPs was measured by Microplate Reader (Ex: 640 nm / Em: 680 nm).

## On-demand digestion of HA-derived MNs

HA-based MNs from *in vitro* studies or retrieved from mice were incubated with 10 mM Tris (2-carboxyethyl) phosphine (TCEP) solution in HBBS at pH 7.4 under rotation at 37°C for 5 minutes. The recovered cellular suspension was filtered with a 70  $\mu$ m cell strainer (BD bioscience) to remove any impurities and further processed by flow cytometry.

## Animal Experiments

Female C57Bl/6 mice (6–8 weeks old) were purchased from Charles River. Mouse procedures were conducted at the Koch Institute for Integrative Cancer Research at the Massachusetts Institute of Technology (MIT) under the protocol approved for this study by the Institutional Animal Care and Use Committee (IACUC). Intravital microscopy studies were performed at the Massachusetts General Hospital under a protocol approved for this study by the Institutional Animal Care and Use Committee (IACUC), using female C57BL/6J mice (8–12 weeks old) provided by Jackson Labs.

### **In vivo therapeutic efficacy and survival studies**

Two different tumor models were used. For mApple-expressing MC38 cells,  $1 \times 10^6$  in 100  $\mu\text{L}$  of HBSS were injected subcutaneously into the right flank of the mice. For orthotopic B16-F10 cells,  $5 \times 10^5$  in 50  $\mu\text{L}$  of HBSS were injected transdermally into the right side of the mice. Five days post-tumor induction, mice were administered empty MNs (as control group), or CpG-NP loaded MNs (treatment group) 5 times, three days apart ( $n = 10$  mice per group). MNs were administered on top of the tumor by thumb-pressing them against the skin or in the surrounding areas and secured with medical-grade tape (FlexCon, USA). MNs were retrieved 24 h post-administration. Tumor size was measured every other day via caliper measurements ( $n = 6$ ), and the tumor volume was calculated using the equation  $V = (\text{Length} \times \text{Width} \times \text{Height})/\pi \div 6$ . Body weight was measured contemporaneously with tumor volume. Mice were euthanized when tumors reached a volume of  $1000 \text{ mm}^3$  or when poor body conditions were observed following the guidelines.

*Immunophenotyping analysis in the TME:* Subcutaneous MC38 tumors were established in female C57Bl/6 mice (6–8 weeks old) as previously described and two studies were conducted. Mechanistic analyses were performed after mice were administered CpG-NP loaded MNs (1  $\mu\text{g}$  delivered per patch) or empty MNs either once or five times (day two and day 20-post treatment initiation, respectively) depending on the cellular populations of interest. To test the diagnostic potential of the MNs, a single dose of CpG-NPs (1  $\mu\text{g}$ ) was administered intratumorally. On the day of mechanistic analysis, tumors were harvested, chopped into  $< 0.5 \text{ mm}$  fragments, and digested in a solution of HBSS supplemented with collagenase I, II, and IV (100 ng/mL), and DNase I (100  $\mu\text{g}/\text{mL}$ ) for 2 h at  $37^\circ\text{C}$ . tdLNs were harvested and mechanically dissociated. Single-cell suspensions of tumors and tdLNs were filtered through a 40  $\mu\text{m}$  nylon cell strainer. Tumor cells were further treated with ACK Lysing Buffer (Gibco) for 1 min. Cells were washed, filtered through a 40  $\mu\text{m}$  nylon cell strainer, and counted. MNs recovered from mice were digested as described before. The following anti-mouse antibodies were used for flow cytometry were purchased from BioLegend: CD45 APC-Cy7 (clone 30-F11), NK-1.1 BV711 (clone PK136), CD45 BV785 (clone 30-F11), CD11b BV421 (clone M1/70), CD86 BV510 (clone GL-1), CD80 BV711 (clone 16-10A1), CD206 PE (clone C068C2), MHCII BV605 (clone M5/114.15.2), CD11c APC (clone N418). The following anti-mouse antibodies were purchased from BD Biosciences: CD3 BB700 (clone 17A2), CD4 BUV395 (clone GK1.5), CD8a BUV737 (clone 53 - 6.7), F4/80 BUV395 (clone T45-2342), CD80 BUV737 (clone 16-10A1). Live cells were gated using LIVE/DEADTM (Thermo Fisher) aqua (cat. no. L34966), green (cat. no. L34970), or near-IR (cat. no. L34976). Stained cells were analyzed by flow cytometry using a BD

LSRFortessa™ flow cytometer (BD Biosciences), and all data were analyzed using FlowJo software (Flowjo LLC).

### **Cytokine analysis**

Half of the harvested tumors for immunophenotyping on day two were processed to analyze the cytokine/chemokines expression profile. Tissues were homogenized with T-PER™ Tissue Protein Extraction Reagent (Thermo Fisher Scientific, cat. no. 78510) containing 1% Halt protease and phosphatase inhibitors (Thermo Fisher Scientific, cat. no. 78442). Then, the samples were incubated at 4°C for 30 min following centrifugation to remove the cell/tissue debris. The supernatant was collected for total protein quantification and cytokine analysis. Levels of IFN $\gamma$ , CCL2 (MCP-1), CXCL1 (KC), and IL-1b were analyzed using a custom Legendplex™ panel (BioLegend) as per the manufacturer's instructions.

### **Analysis of tumor proliferation by immunohistochemistry**

Skin tissue sections were processed and imaged by the Hope Babette Tang Histology facility at the Koch Institute of Integrative Cancer Research at MIT (Cambridge, USA). Briefly, 1 cm<sup>3</sup> tumor sections were harvested on the day of mechanistic analysis were embedded in O.C.T. in plastic base molds for tissue embedding. Samples were flash-frozen in a dry ice bath and preserved at -80°C until sectioning. Tumors were cryosectioned into 20  $\mu$ m-wide tissue sections, and proliferation was assessed via H&E and Ki-67 staining. The microscopic images were processed using the Aperio ImageScope 12.3.3 software (Leica).

### **Intravital microscopy**

In vivo microscopy was performed using an Olympus FV1000 multiphoton/confocal imaging system following procedures described previously [40,50]. Animals were used with Institutional Subcommittee on Research Animal Care guidelines. 5 x 10<sup>5</sup> MC38-H2B-mApple cells in 50  $\mu$ L PBS were injected under the fascia two days after DSWC implantation surgery and imaged ~ 7 days later upon tumor formation. MN patches were applied onto the tissue within the window chamber, and glass coverslips were replaced over the patch to protect the tissue. Twenty-four hours later, patches were removed, and tissue was imaged after adding saline and replacing the coverslip. An XLFluor  $\times$ 2 air objective (numerical aperture 0.14, Olympus) was used for low-magnification imaging of the entire tumor and MN delivery region.

In contrast, higher-magnification imaging was conducted with an XLUMPLFLN  $\times$ 20 water immersion objective (numerical aperture, 1.0, Olympus). Sequentially scanned images were acquired with 559- and 633-nm diode lasers and a DM405/488/559/635-nm dichroic beam splitter [40,50]. Empty patches lacking both CpG and dye were re-applied under coverslips for 24 h repeated twice to mirror the serial treatment scheme in the subcutaneous experiments (above). Longitudinal imaging was performed for up to 9 days post-treatment.

**Statistical Analysis:** Statistical analyses were performed using Graph-Pad Prism 8 (GraphPad Software). For in vitro experiments, a minimum of  $n = 3$  biological replicates were used per condition in each experiment. The unpaired Student's t-test evaluated the statistical difference between the two measurements. A Post hoc test for one-way ANOVA was used to test the statistical difference between sets of measurements. For in vivo experiments, a minimum of  $n = 4$  biological replicates were used per condition in each experiment. Multiple comparisons among groups were determined using a non-parametric t-test. No specific pre-processing of data was performed before statistical analyses. Differences between groups were considered significant at p-values below 0.05 (\*  $p < 0.05$ , \*\*  $p < 0.01$ , \*\*\*  $p < 0.001$ ).

## Declarations

Competing interests: The authors declare no competing interests.

Acknowledgments:

This work was supported in part by NIH grants DP2CA259675 (MAM) and U01CA206997 (RW). The authors thank the Swanson Biotechnology Center at the Koch Institute for Integrative Cancer Research at the Massachusetts Institute of Technology (MIT) for assistance with animal experiments and facilities, especially the flow cytometry core. The authors thank G. Paradis for FACS assistance with Cancer Center Support (FACS core). The authors thank Rainer H. Kohler, Ph.D. (Massachusetts General Hospital), for their expertise and service in microscopy experiments. RW is a consultant to ModeRNA, Tarveda Pharmaceuticals, Lumicell, Seer, Earli, Aikili Biosystems, and Accure Health. MAM is a scientific advisor for January Therapeutics and has received past support from Ionis Pharmaceuticals, Pfizer, and via material transfer agreement from Genentech/Roche. None of these activities are related to the manuscript. Figures were created with BioRender.com.

## References

1. Prausnitz MR. Microneedles for transdermal drug delivery. *Advanced Drug Delivery Reviews*. 2004; 56: 581–7.
2. Ita K. Transdermal Delivery of Drugs with Microneedles-Potential and Challenges. *Pharmaceutics*. 2015; 7: 90–105.
3. Moreira AF, Rodrigues CF, Jacinto TA, Miguel SP, Costa EC, Correia IJ. Microneedle-based delivery devices for cancer therapy : A review. *Pharmacological Research*. 2019; 148: 1–11.
4. Singh V, Kesharwani P. Recent advances in microneedles-based drug delivery device in the diagnosis and treatment of cancer. *Journal of Controlled Release*. 2021; 338: 394–409.

5. Karapetayan L, Luke JJ, Davar D. Toll-Like Receptor 9 Agonists in Cancer. *OncoTargets and Therapy*. 2020; 13: 10039–60.
6. Irvine DJ, Dane EL. Enhancing cancer immunotherapy with nanomedicine. *Nat Rev Immunol*. 2020; 20: 321–34.
7. Milling L, Zhang Y, Irvine DJ. Delivering safer immunotherapies for cancer. *Advanced Drug Delivery Reviews*. 2017; 114: 79–101.
8. Riley RS, June CH, Langer R, Mitchell MJ. Delivery technologies for cancer immunotherapy. *Nat Rev Drug Discov*. 2019; 18: 175–96.
9. Turner JG, White LR, Estrela P, Leese HS. Hydrogel-Forming Microneedles: Current Advancements and Future Trends. *Macromolecular Bioscience*. 2021; 21: 1–18.
10. Wang PM, Cornwell M, Prausnitz MR. Minimally Invasive Extraction of Dermal Interstitial Fluid for Glucose Monitoring Using Microneedles. *Diabetes Technology & Therapeutics*. 2005; 7: 131–41.
11. al Sulaiman D, Chang JYH, Bennett NR, et al. Hydrogel-Coated Microneedle Arrays for Minimally Invasive Sampling and Sensing of Specific Circulating Nucleic Acids from Skin Interstitial Fluid. *ACS Nano*. 2019; 13: 9620.
12. Wiig H, Swartz MA. Interstitial fluid and lymph formation and transport: physiological regulation and roles in inflammation and cancer. *Physiol Rev*. 2012; 92: 1005–60.
13. Samant PP, Niedzwiecki MM, Raviele N, et al. Sampling interstitial fluid from human skin using a microneedle patch. *Science Translational Medicine*. 2020; 12: 1–16.
14. Wiig H, Tenstad O, Iversen PO, Kalluri R, Bjerkvig R. Interstitial fluid: the overlooked component of the tumor microenvironment? *Fibrogenesis & Tissue Repair*. 2010; 3.
15. Zhu J, Zhou X, Kim HJ, et al. Gelatin Methacryloyl Microneedle Patches for Minimally Invasive Extraction of Skin Interstitial Fluid. *Small*. 2020; 16: 1905910.
16. Rudqvist N, Pilonis KA, Lhuillier C, Wennerberg E. Radiotherapy and CTLA-4 blockade shape the TCR repertoire of tumor-infiltrating cells. *Cancer Immunology Research*. 2019; 6: 139–50.
17. Celis JE, Gromov P, Cabezón T, et al. Proteomic characterization of the interstitial fluid perfusing the breast tumor microenvironment. *Molecular and Cellular Proteomics*. 2004; 3: 327–44.
18. Espinoza JA, Jabeen S, Batra R, et al. Cytokine profiling of tumor interstitial fluid of the breast and its relationship with lymphocyte infiltration and clinicopathological characteristics. *Oncoimmunology* [Internet]. 2016; 5: e1248015 (14. Available at: <https://doi.org/10.1080/2162402X.2016.1248015>

19. Chen L, Zhang C, Xiao J, et al. Local extraction and detection of early stage breast cancers through a microneedle and nano-Ag/MBL film based painless and blood-free strategy. *Materials Science and Engineering C*. 2020; 109.
20. He R, Niu Y, Li Z, et al. A Hydrogel Microneedle Patch for Point-of-Care Testing Based on Skin Interstitial Fluid. *Advanced Healthcare Materials*. 2020; 9: 1–11.
21. Zheng M, Wang Z, Chang H, et al. Osmosis-Powered Hydrogel Microneedles for Microliters of Skin Interstitial Fluid Extraction within Minutes. *Advanced Healthcare Materials*. 2020; 9: 1–11.
22. Mandal A, Boopathy A v., Lam LKW, et al. Cell and fluid sampling microneedle patches for monitoring skin-resident immunity. *Science Translational Medicine*. 2018; 10.
23. Puigmal N, Dosta P, Solhjou Z, et al. Microneedle-Based Local Delivery of CCL22 and IL-2 Enriches T reg Homing to the Skin Allograft and Enables Temporal Monitoring of Immunotherapy Efficacy. *Advanced Functional Materials*. 2021; 31: 1–12.
24. Mellman I, Coukos G, Dranoff G. Cancer immunotherapy comes of age. *Nature*. 2011; 480: 480–9.
25. Hargadon KM, Johnson CE, Williams CJ. Immune checkpoint blockade therapy for cancer: An overview of FDA-approved immune checkpoint inhibitors. *International Immunopharmacology*. 2018; 62: 29–39.
26. Hanagata N. CpG oligodeoxynucleotide nanomedicines for the prophylaxis or treatment of cancers, infectious diseases, and allergies. Vol. 12, *International Journal of Nanomedicine*. Dove Medical Press Ltd.; 2017.
27. Dosta P, Ramos V, Borrós S. Stable and efficient generation of poly( $\beta$ -amino ester)s for RNAi delivery. *Molecular Systems Design & Engineering*. 2018; 3: 677–89.
28. Dosta P, Segovia N, Cascante A, Ramos V, Borrós S. Surface charge tunability as a powerful strategy to control electrostatic interaction for high efficiency silencing, using tailored oligopeptide-modified poly( $\beta$ -amino ester)s (PBAEs). *Acta Biomaterialia*. 2015; 20: 82–93.
29. Segovia N, Dosta P, Cascante A, Ramos V, Borrós S. Oligopeptide-terminated poly ( $\beta$ -amino ester) s for highly efficient gene delivery and intracellular localization. *Acta Biomaterialia*. 2014; 10: 2147–58.
30. Dosta P, Tamargo I, Ramos V, et al. Delivery of Anti-microRNA-712 to Inflamed Endothelial Cells Using Poly( $\beta$ -amino ester) Nanoparticles Conjugated with VCAM-1 Targeting Peptide. *Advanced Healthcare Materials*. 2021; e2001894.
31. Dosta P, Demos C, Ramos V, et al. Delivery of siRNA to Endothelial Cells In Vivo Using Lysine/Histidine Oligopeptide-Modified Poly( $\beta$ -amino ester) Nanoparticles. *Cardiovascular Engineering and Technology*. 2021; 12: 114–25.

32. Latz E, Schoenemeyer A, Visintin A, et al. TLR9 signals after translocating from the ER to CpG DNA in the lysosome. *Nature Immunology*. 2004; 5: 190–8.
33. Buss CG, Bhatia SN. Nanoparticle delivery of immunostimulatory oligonucleotides enhances response to checkpoint inhibitor therapeutics. *Proc Natl Acad Sci U S A*. 2020; 117: 13428–36.
34. Yuan S, Qiao T, Chen W. CpG Oligodeoxynucleotide 1826 Enhances the Lewis Lung Cancer Response to Radiotherapy in Murine Tumor. *Cancer Biotherapy and Radiopharmaceuticals*. 2011; 26.
35. Taniguchi K, Karin M. NF- $\kappa$ B, inflammation, immunity and cancer: Coming of age. *Nature Reviews Immunology*. 2018; 18: 309–24.
36. Madaan A, Verma R, Singh AT, Jain SK, Jaggi M. A stepwise procedure for isolation of murine bone marrow and generation of dendritic cells. *Journal of Biological Methods*. 2014; 1: e1.
37. Huang L, Xu H, Peng G. TLR-mediated metabolic reprogramming in the tumor microenvironment: potential novel strategies for cancer immunotherapy. *Cellular and Molecular Immunology*. 2018; 15: 428–37.
38. Samarasinghe R, Tailor P, Tamura T, Kaisho T, Akira S, Ozato K. Induction of an Anti-Inflammatory Cytokine, IL-10, in Dendritic Cells After Toll-like Receptor Signaling. Vol. 26, *Journal of interferon & cytokine research*. 2006.
39. Switaj T, Jalili A, Jakubowska AB, et al. CpG immunostimulatory oligodeoxynucleotide 1826 enhances antitumor effect of interleukin 12 gene-modified tumor vaccine in a melanoma model in mice. *Clinical Cancer Research*. 2004; 10: 4165–75.
40. Arlauckas SP, Garris CS, Kohler RH, et al. In vivo imaging reveals a tumor-associated macrophage-mediated resistance pathway in anti-PD-1 therapy. *Science Translational Medicine*. 2017; 9.
41. Lu H. TLR agonists for cancer immunotherapy: Tipping the balance between the immune stimulatory and inhibitory effects. *Frontiers in Immunology*. 2014; 5: 3–6.
42. Noh JY, Yoon SR, Kim TD, Choi I, Jung H. Toll-Like Receptors in Natural Killer Cells and Their Application for Immunotherapy. Vol. 2020, *Journal of Immunology Research*. Hindawi Limited; 2020.
43. Darvin P, Toor SM, Nair VS, Elkord E. Immune checkpoint inhibitors: recent progress and potential biomarkers. *Experimental & Molecular Medicine*. 2018; 12: 1–11.
44. Arlauckas SP, Garren SB, Garris CS, et al. Arg1 expression defines immunosuppressive subsets of tumor-associated macrophages. *Theranostics*. 2018; 8: 5842–54.
45. Harlin H, Meng Y, Peterson AC, et al. Chemokine expression in melanoma metastases associated with CD8 + T-Cell recruitment. *Cancer Research*. 2009; 69: 3077–85.

46. Sideras K, Galjart B, Vasaturo A, et al. Prognostic value of intra-tumoral CD8+/FoxP3+ lymphocyte ratio in patients with resected colorectal cancer liver metastasis. *Journal of Surgical Oncology*. 2018; 118: 68–76.
47. Pagès F, Galon J, Dieu-Nosjean MC, Tartour E, Sautès-Fridman C, Fridman WH. Immune infiltration in human tumors: A prognostic factor that should not be ignored. *Oncogene*. 2010; 29: 1093–102.
48. Diederichsen ACP, Hjelmberg JVB, Christensen PB, Zeuthen J, Fenge C. Prognostic value of the CD4+/CD8+ ratio of tumour infiltrating lymphocytes in colorectal cancer and HLA-DR expression on tumour cells. *Cancer Immunology, Immunotherapy*. 2003; 52: 423–8.
49. Postow MA, Callahan MK, Wolchok JD. Immune Checkpoint Blockade in Cancer Therapy. *Journal of Clinical Oncology*. 2015; 33.
50. Luthria G, Li R, Wang S, et al. In vivo microscopy reveals macrophage polarization locally promotes coherent microtubule dynamics in migrating cancer cells. *Nature Communications*. 2020; 11.

## Figures

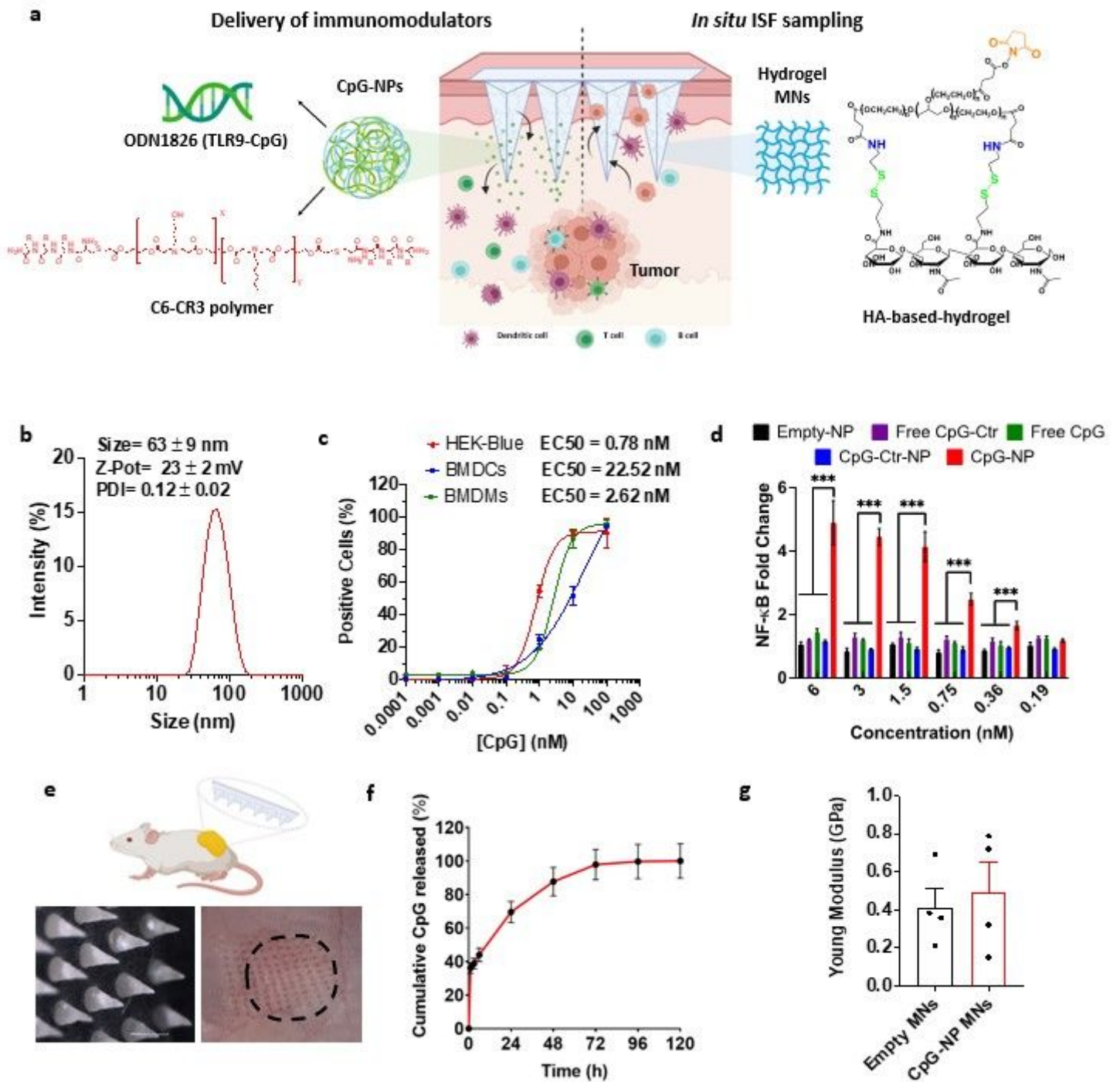


**Figure 1**

**Engineering a theranostic microneedle platform for the management of skin cancer.** **a**, Representative scheme of a hyaluronic acid (HA)-based microneedle platform for the delivery of immunomodulatory drugs (CpG-ODNs) complexed with poly (beta-amino ester)s (PBAEs) and simultaneous sampling of interstitial fluid (ISF) for recovery of immune cells *ex vivo*. **b**, Biophysical characterization of CpG-containing nanoparticles as determined by dynamic light scattering. **c**, Quantification by flow cytometry of the cellular internalization of CpG-NPs by TLR9-expressing HEK 293 cells, bone marrow-derived dendritic cells (BMDCs), and bone marrow-derived macrophages (BMDMs) *in vitro* (n = 3 biologically

independent samples). **d**, Dose-response of NF- $\kappa$ B produced by CpG-NP, CpG-Ctr-NP and empty-NP in HEK293 TLR9 reporter cell line *in vitro* (n = 4 biologically independent samples). **e**, Micrograph of the HA-based MNs (scale bar = 500  $\mu$ m) and representative image of mouse skin after *in vivo* administration of hydrogel MNs into the tumor, five days post-tumor induction. The dotted area indicates the tumor site. **f**, *In vitro* CpG-NP release profile from the MNs assessed by tracking the fluorescence intensity of labeled nanoparticles over time (pH = 7.4, 37°C). Data are means  $\pm$  s.e.m. (n = 4). **g**, Characterization of the mechanical properties of HA-based MNs. A compression test was performed to compare the mechanical strength of empty MNs versus CpG-NP loaded MNs. Data are means  $\pm$  s.e.m. (n = 4).

**Figure 2**

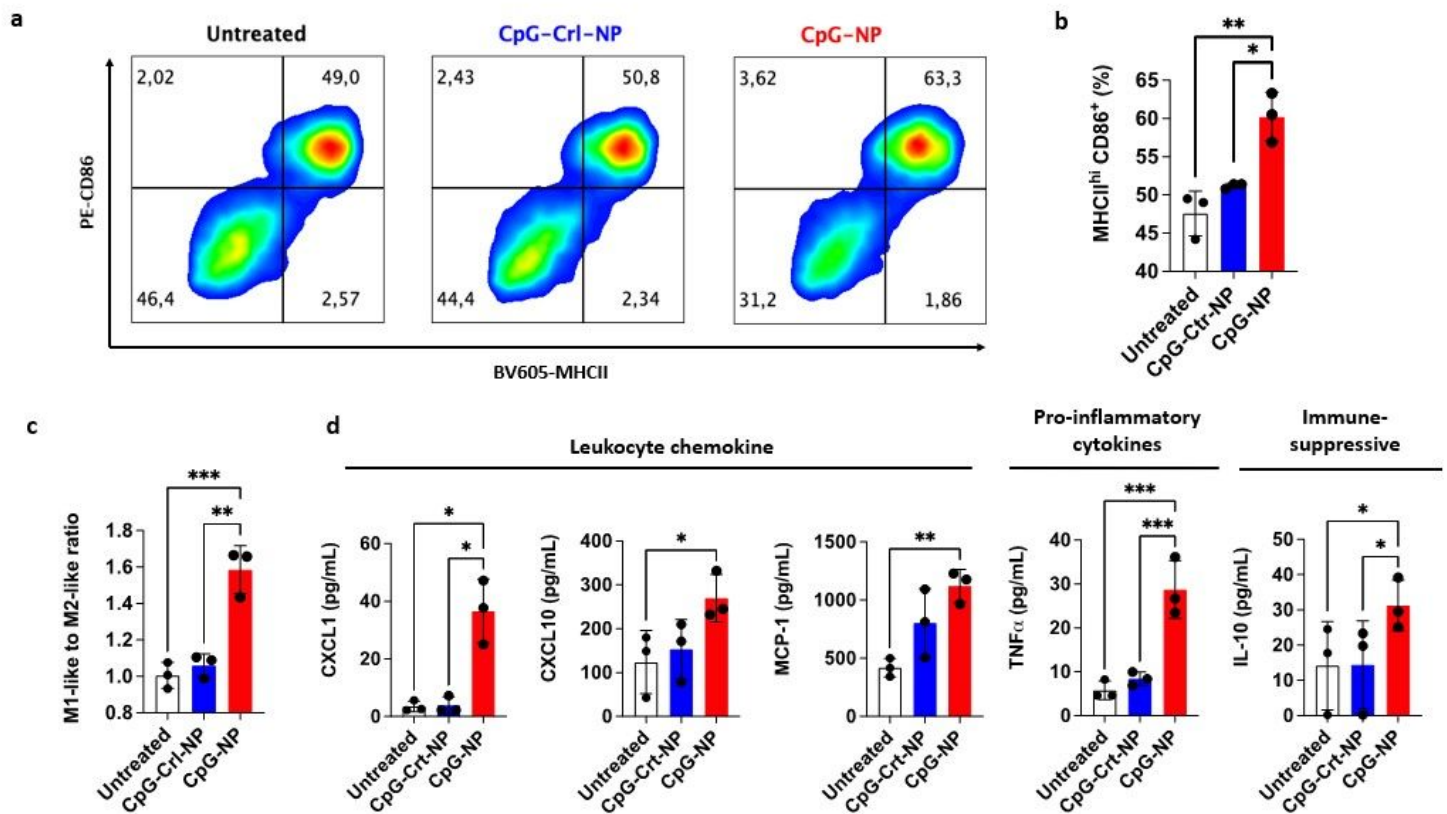


**Figure 2**

**CpG-NPs activate innate immune cells in vitro.** **a**, Representative flow cytometry density plot of MHCII and CD86 expression in BMDCs treated with CpG-NP or CpG-Ctr-NP at 10nM (red denotes higher cell density). **b**, Flow cytometry quantification of MHCII<sup>hi</sup> CD86<sup>+</sup> expression in BMDCs 24 h following CpG-NP or CpG-Ctr-NP treatment at 10 nM. Data are means  $\pm$  s.e.m. (n = 3). **c**, Flow cytometry quantification of CD86<sup>+</sup> / CD206<sup>+</sup> (M1-like to M2-like ratio) 24 h following CpG-NP or CpG-Ctr-NP treatment at 10nM, in CD11b<sup>+</sup> F4/80<sup>+</sup> cells. Data are means  $\pm$  s.e.m (n = 3). **d**, Protein analysis of conditioned media supernatant, 24 h after treatment with CpG-NP or CpG-Ctr-NP in BMDMs. Data are means  $\pm$  s.e.m (n=5 samples per group). \*\*\*P< 0.001, \*\*P<0.01, \*P<0.05.

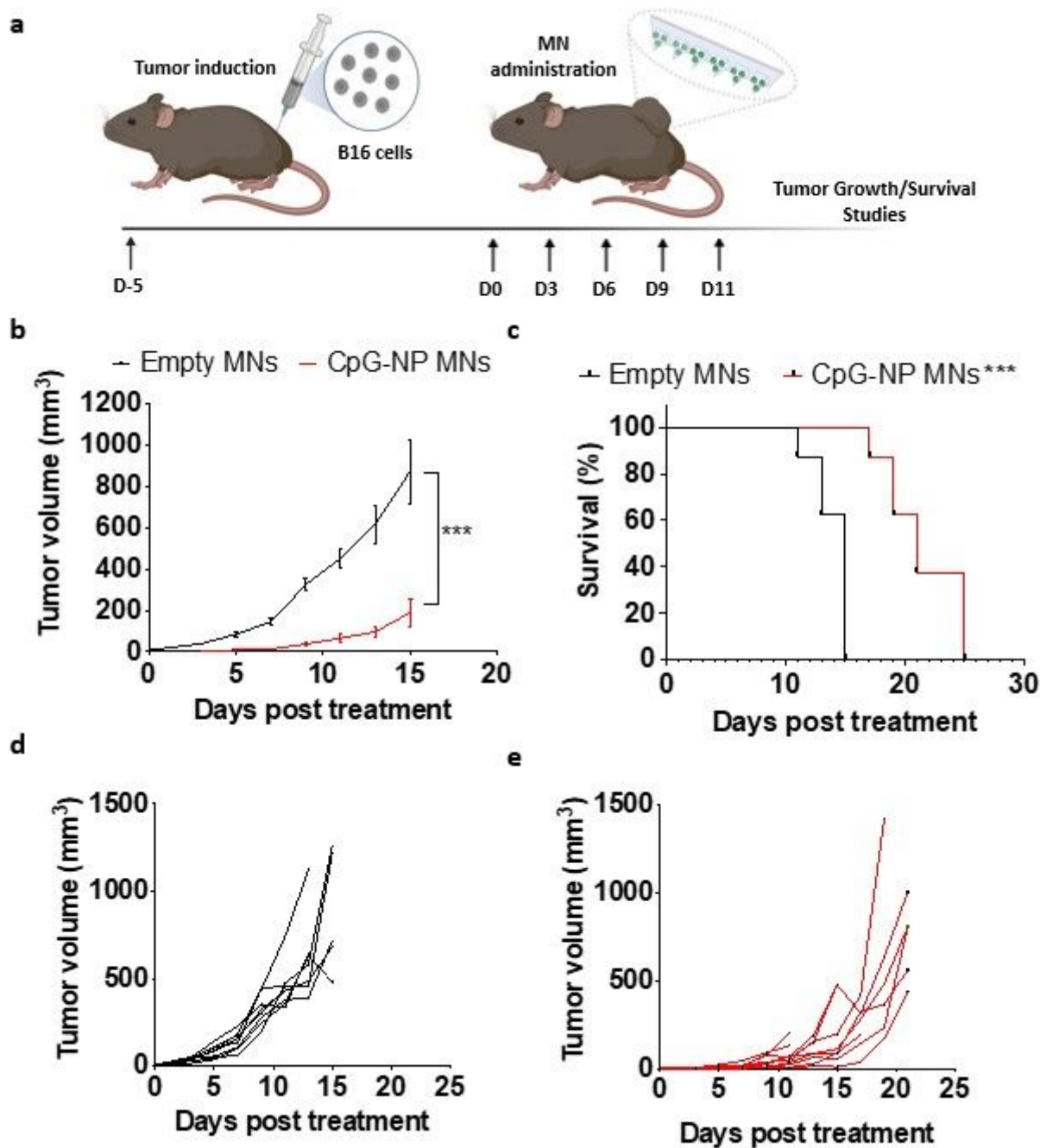


**Figure 3**

**Transdermal delivery of CpG-NPs using MNs reduces tumor growth and increases survival in a murine model of orthotopic melanoma.** **a**, Five days post tumor implantation, orthotopic tumors were administered with MNs loaded with CpG-NPs (1  $\mu$ g CpG-ODN) or empty MNs (control group). MNs were applied on top of the tumor every three days for five cycles (q3dx5). **b**; Tumor growth in B16-F10 melanoma-bearing mice. (n= 8-10, data are means  $\pm$  s.e.m.). **c**, Kaplan-Meier curves of humane survival. Statistical significance was determined against the control group by the Mantel-Cox test. \*\*\*P < 0.001, \*\*P < 0.01, \*P < 0.05. **d-e**, Individual tumor growth curves of empty MNs (d) and CpG-NP MNs (e) treatment groups. n = 8-10 biologically independent samples.

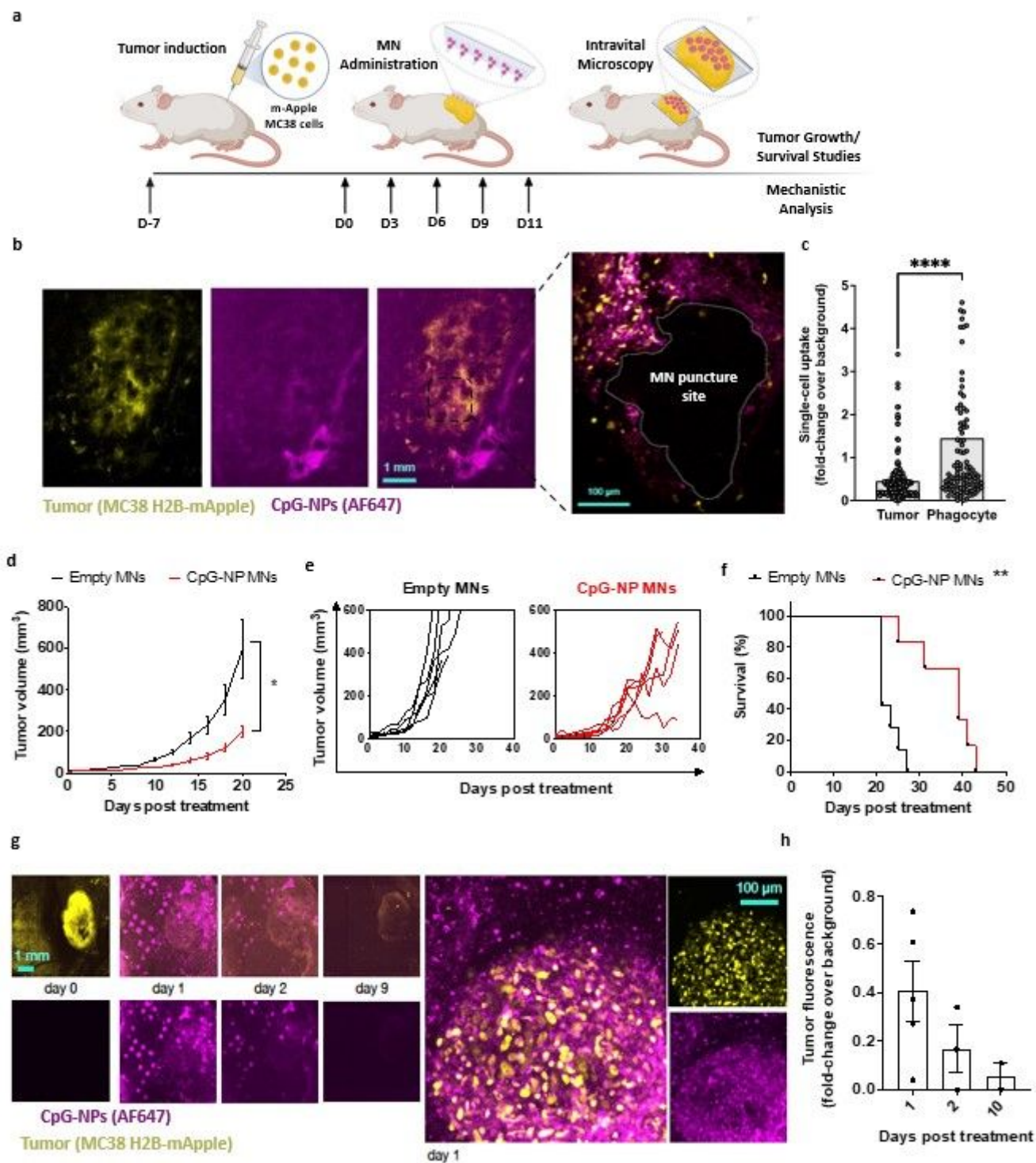


**Figure 4**

**Intravital microscopy (IVM) reveals the spatial-temporal localization of CpG-NPs in the TME following MN transdermal delivery, as well as their therapeutic efficiency.** **a**, Experimental design of the *in vivo* studies. **b**, IVM of mApple expressing MC38 tumors (yellow) treated with fluorescent CpG-NPs (magenta) loaded in the MNs. MNs were applied to the mApple MC38 tumors for 24h and removed before IVM imaging. **c**, Single cell uptake quantification of CpG-NPs by IVM. Data are means  $\pm$  s.e.m. **d-f**, Mice with subcutaneous MC38-mApple tumors were treated seven days post-tumor induction with empty MNs or MNs loaded with CpG-NPs (1  $\mu$ g CpG-ODN) three days apart for five cycles (q3dx5), with tumor growth

measured by caliper and shown as averages (d), individual growth curves (e), and Kaplan-Meier humane survival curves (n= 8-10, data are means  $\pm$  s.e.m.). Statistical significance was determined against the control-treated group by the Mantel-Cox test. \*\*\*P < 0.001, \*\*P < 0.01, \*P < 0.05. **g**, IVM of MC38-mApple tumors (yellow) treated with fluorescent CpG-NPs (magenta) (left, scale bar: 1mm; right, scale bar: 100 $\mu$ m). **h**, mApple tumor fluorescence over time, measured by IVM (n= 2-5, data are means  $\pm$  s.e.m.).

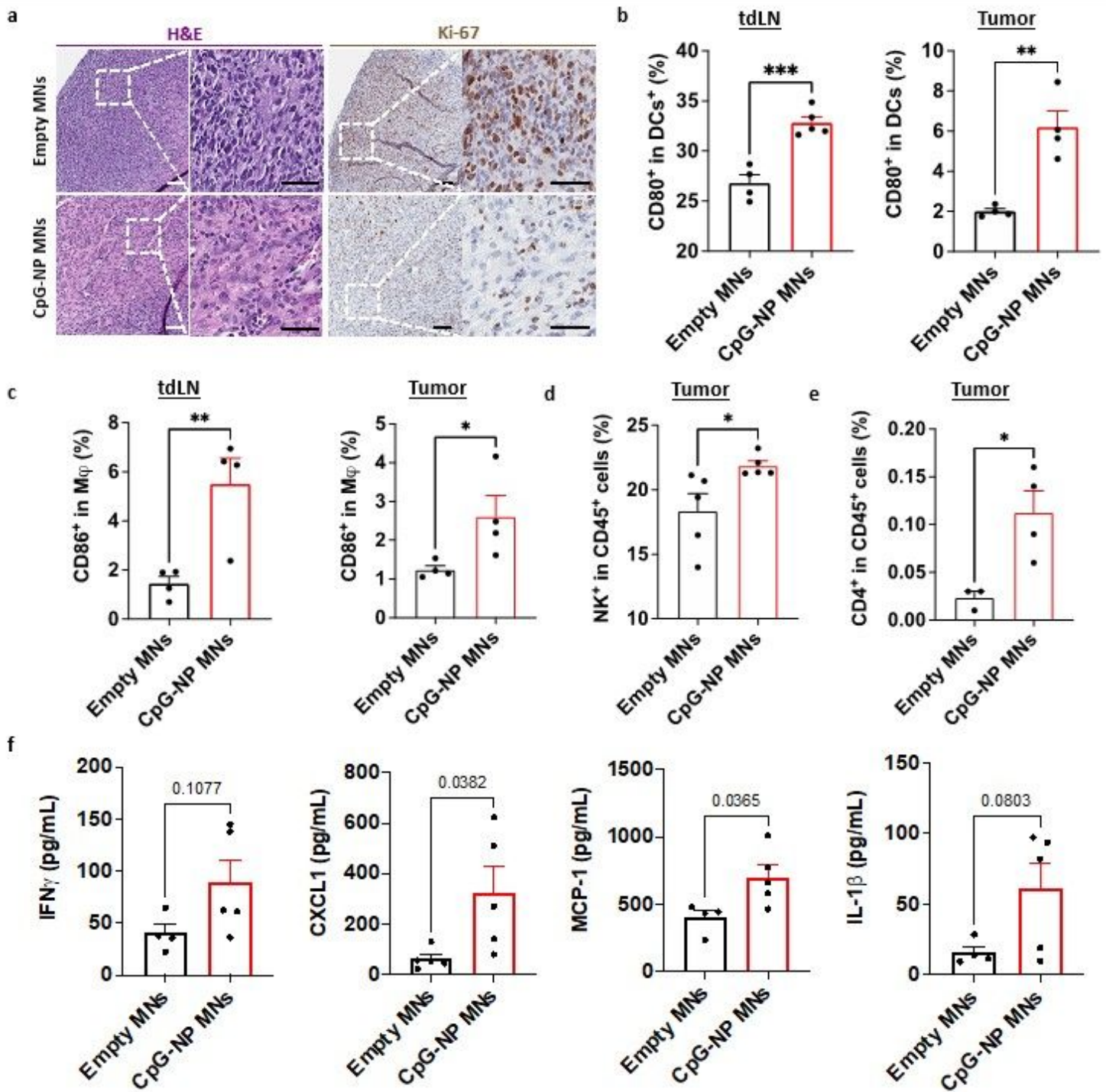
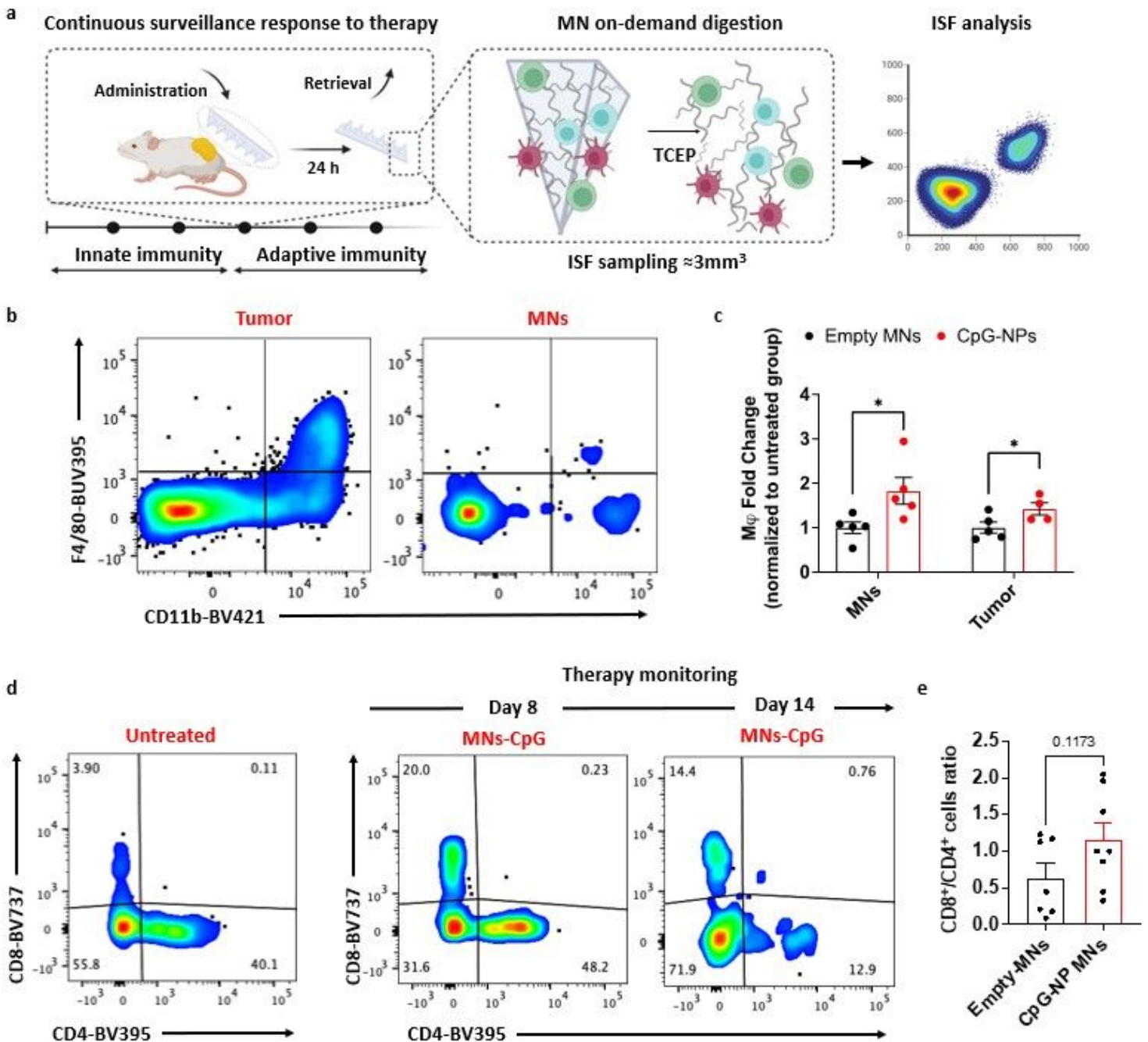


Figure 5

**Delivery of CpG-NPs using microneedles modulates the immune composition in the TME. a,**

Representative H&E staining (left, scale bar: 100  $\mu\text{m}$ ; right: scale bar: 50  $\mu\text{m}$ ) and Ki-67 staining (left, scale bar: 100  $\mu\text{m}$ ; right: scale bar: 50  $\mu\text{m}$ ) in MC38 tumors harvested on day 20 post-tumor induction (n = 5). **b,** Flow cytometry quantification of activated dendritic cells (CD80<sup>hi</sup> CD11c<sup>+</sup>MHCII<sup>+</sup>CD45<sup>+</sup>) in tdLNs (left) and tumors (right) 48 h post transdermal delivery of CpG-NPs. Data are means  $\pm$  s.e.m. (n = 5). **c,** Flow cytometry quantification in the tdLNs (left) and tumors (right) of activated macrophages (CD86<sup>hi</sup> F4/80<sup>+</sup>CD11b<sup>+</sup>CD45<sup>+</sup>) 48 h following MN-mediated delivery of CpG-NPs. Data are means  $\pm$  s.e.m. (n = 5). **d,e,** Flow cytometric quantification of the percentage of natural killer cells (d) and CD4<sup>+</sup> cells (e) in tumor lysates 48 h post-treatment with CpG-NPs. **f,** Analysis of the pro-inflammatory cytokine/chemokine profile in tumors using a bead-based immunoassay (Legendplex™). Data are means  $\pm$  s.e.m. (n = 5). \*\*\*P < 0.001, \*\*P < 0.01, \*P < 0.05.



**Figure 6**

**Serial monitoring of the immune composition of the TME in ISF using HA-based MNs.** **a**, Scheme of MN immune cell sampling. After a single-dose injection of CpG-NPs, MNs were administered and digested with TCEP for subsequent analysis of the cellular immune signature compared to that from tumor lysates by flow cytometry. **b**, **c**, Flow cytometry dot plot (left) and quantification of macrophages (CD11b<sup>+</sup> F4/80<sup>+</sup>) (right) recovered with MNs at 2d following treatment. Data are means  $\pm$  s.e.m. ( $n = 4-5$ ). \*\*\* $P < 0.001$ , \*\* $P < 0.01$ , \* $P < 0.05$ . **d**, Serial monitoring of T cell infiltrates in ISF following treatment with CpG-NP MNs. **e**, Representative dot plot of CD8<sup>+</sup> and CD4<sup>+</sup> T cell populations over time from MN-sampled ISF.

**f**, Ratio of CD8<sup>+</sup> to CD4<sup>+</sup> T cells extracted with MNs representing pooled values from day 11 and day 14 post-treatment initiation. Data are means  $\pm$  s.e.m. (n = 7-8). \*\*\*P < 0.001, \*\*P < 0.01, \*P < 0.05.

## Supplementary Files

This is a list of supplementary files associated with this preprint. Click to download.

- [SupplementaryinformationMNsXCancerArtzi.docx](#)